Evidence of Unique Stacking and Related Topological Defects in the Honeycomb Layered Oxide: $K_2Ni_2TeO_6$

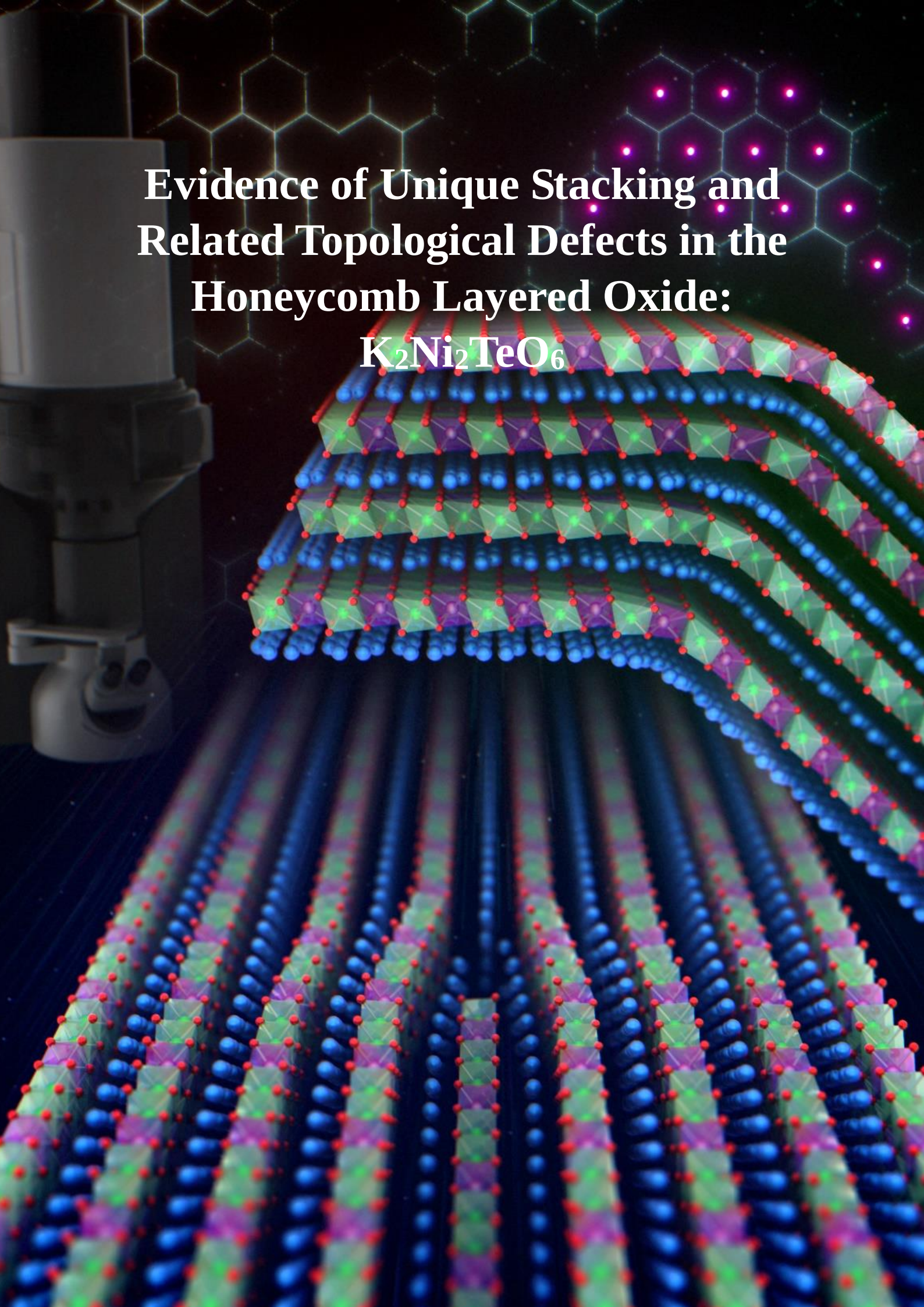

Titus Masese[a,b], Yoshinobu Miyazaki[c], Godwill Mbiti Kanyolo[d], Teruo Takahashi[c], Miyu Ito[c], Hiroshi Senoh[a] & Tomohiro Saito[c]

[a] Research Institute of Electrochemical Energy, National Institute of Advanced Industrial Science and Technology (AIST), 1–8–31 Midorigaoka, Ikeda, Osaka 563–8577, JAPAN

[b] AIST–Kyoto University Chemical Energy Materials Open Innovation Laboratory (ChEM–OIL), Sakyo–ku, Kyoto 606–8501, JAPAN

[c] Tsukuba Laboratory, Technical Solution Headquarters, Sumika Chemical Analysis Service (SCAS), Ltd., Tsukuba, Ibaraki 300–3266, JAPAN

[d] Department of Engineering Science, The University of Electro-Communications, 1–5–1 Chofugaoka, Chofu, Tokyo 182–8585, JAPAN

Correspondence to: titus.masese@aist.go.jp

Abstract

Endowed with a multitude of exquisite properties such as rich electrochemistry, superb topology and eccentric electromagnetic phenomena, honeycomb layered oxides have risen to the top echelons of science with applications in diverse fields ranging from condensed matter physics, solid-state chemistry, materials science, solid-state ionics to electrochemistry. Although these features are known to stem from the utilitarian structure innate in these oxides, their functionalities are vastly underutilised as their underlying atomistic mechanisms remain unknown. Therefore, in this study, atomic-resolution imaging on pristine $K_2Ni_2TeO_6$ along multiple zone axes were conducted using spherical aberration-corrected scanning transmission electron microscopy (Cs-corrected STEM) to reveal hitherto unreported topological defects and curvature which can be associated with various phase transitions. Furthermore, we discover, for the first time, the occurrence of a new stacking variant with P3-type sequence alongside the well-reported P2-type stacking domains. Through this work, we provide insights into the connection between these unique structural disorders to the electrochemical properties of honeycomb layered oxides. The mechanism of the phase transitions reported herein is bound to become apparent upon high alkali-ion mobility, providing invaluable clues to potentially improve their functional performance in, for instance, energy storage applications. Our findings have the potential to inspire further experimental and theoretical studies into the role of stacking and topology in honeycomb layered oxides.

INTRODUCTION

In the quest to find solutions to energy sustainability and ecological challenges, nanotechnology has emerged as the ultimate platform for developing new materials that promise unprecedented revolutions in various facets of civilisation such as transport, communication and energy. [1–3] In the field of energy storage, a burgeoning class of two-dimensional nanostructured materials known as honeycomb layered oxides has drawn enormous interest for their potential as rechargeable battery components. [4–8] This class of layered oxides has been found to exhibit diverse crystal structural frameworks with exceptional electrochemical capabilities and remarkable electromagnetic phenomena making them pertinent as functional battery materials. [9–34] As with other nanostructured materials, the advancement of these layered oxides depends on the manipulation of matter at a mesoscopic level to tailor desirable functionalities for improved performance and to expand their range of applications. As such, the understanding of their chemical compositions, crystal frameworks and topological orders and defects remains pertinent for their development.

From a chemical composition perspective, honeycomb layered oxides generally adopt the following stoichiometric chemical compositions: $A_2M_2DO_6$, $A_3M_2DO_6$ and A_4MDO_6 (where *M* can be divalent or trivalent transition metal atoms such as Cr, Mn, Fe, Co, Ni, Cu or some combination thereof; *D* represents pentavalent or hexavalent metal atoms such as Nb, Mo, Ru, Sb, Te, Ta, W, Ir, Bi ; and *A* can be alkali atoms such as Li, Na, K, *et cetera*. or coinage-metal atoms such as Cu, Ag, *et cetera*). [4–31] Given the differences in both the valency state and ionic radius between *M* and *D*, the 2:1 atomic ratio between *M* and *D* atoms in compositions (such as in $A_2M_2DO_6$ and $A_3M_2DO_6$) engenders a distinct honeycomb arrangement of *M* atoms around *D* atoms in the slabs. The resulting heterostructures entail a layered framework with *A* alkali atoms sandwiched between parallel transition metal oxide slabs (MO_6 and DO_6 octahedra). Oxygen atoms from the transition metal oxides in turn coordinate with A^+ cations forming interlayer bonds whose strength is significantly weaker than the covalent in-plane bonds within the transition metal oxide slabs. The magnitude and nature of the interlayer coordination is generally dependent on the Shannon-Prewitt radii of the alkali atoms which dictate the interlayer distance of the emergent configuration.[35]

In fact, a strong correlation between the topology and the resulting physicochemical properties of the honeycomb layered oxides exists that can be traced to the difference in

the sizes of the present A^+ cations. For instance, honeycomb layered oxides with smaller atomic radii cations such as Li atoms in $Li_2Ni_2TeO_6$ tend to form stronger tetrahedral coordinations between Li atoms and oxygen atoms, with 2 repetitive honeycomb layers (comprising NiO_6 and TeO_6 octahedra) for each unit cell.[5] This type of structure is typically referred to as T2-type in the Hagenmuller notation [36] (where 'T' is the tetrahedral coordination and '2' is the number of honeycomb slabs per unit cell). On the other hand, honeycomb layered oxides comprising *A* atoms with larger ionic radii such as Na^+ in $Na_3Ni_2SbO_6$ adopt an O3-type layered framework (where 'O' is an octahedral coordination with a periodicity of three honeycomb slabs per unit cell) whilst Na^+ and K^+ in $Na_2Ni_2TeO_6$ and $K_2Ni_2TeO_6$, respectively, adopt a P2-type framework (where 'P' is a prismatic coordination with a periodicity of two). [8, 11, 15, 16, 29, 44, 49] **Figure 1** shows a compendium of the coordination adopted by *A* alkali atoms in a majority of honeycomb layered oxides reported so far. [5, 8, 11, 15, 31, 37–54] It is worthy to note that for the formation of prismatic coordination (P-type), interlayer distances wider than octahedrally coordinated (O-type) layered oxides are required.[35] Therefore, honeycomb layered oxides containing alkali atoms with larger ionic radii such as K or Rb typically result in P-type configurations.

During alkali-ion (re-)insertion in battery operations, honeycomb layered oxides undergo structural changes which correspond to phase transitions. The extraction of alkali ions during charging, creates voids and vacancies concomitant with an increase in the valency state of divalent transition metal (M^{2+}) and *vice versa* during discharge. This facilitates enhanced expulsion of alkali-ions which further increases the interslab distance, hence inducing additional structural changes in the honeycomb structure. For instance, during the Na-ion extraction from the $Na_3Ni_2SbO_6$ cathode, sequential topological changes are observed with the initial O-type structure with three repetitive honeycomb layers shifting to a P-type structure with 3 consecutive layers.[55] Further repulsion of alkali-ions creates an additional shift from the P3- type structure into an O1-type structure. These rampant changes in the stacking sequences are associated with the manifold electrochemical properties such as staircase-like voltage profiles innate in $Na_3Ni_2SbO_6$ honeycomb layered oxides.[7,15,55]

Although, topological shifts within the layered structures are often postulated to be the underlying elements behind the tessellation of features innate in honeycomb layered oxides, theoretical and experimental explorations into the structure–property relationships remain underdeveloped. The dynamic nature of the structural evolutions

and the inferior stability of these crystal structures, particularly P-type structures, make them difficult not only to synthesise but also to investigate. In fact, amongst honeycomb layered oxides, P3-type structures have only been reported in $Na_3Ni_2SbO_6$ as intermittent products of electrochemical reactions.[7,15,55]

To investigate the structural changes in the crystals, X-ray diffraction (XRD) measurements are conducted on the cathode material after undergoing electrochemical reactions in battery operations to provide information on the long-range periodicity of electron densities of atoms. However, due to limited accuracy, XRD can only provide the average structural information of the crystalline materials during battery operations but fails to account for the short-range structural evolutions occurring immediately after synthesis of the cathode material. Thus, in order to gain a deeper insight into the intermittent stacking evolutions occurring during the electrochemical operations, a thorough comprehension of the initial crystal structure and inherent defects would be essential. As a solution, transmission electron microscopy (TEM) can be employed alongside XRD analyses to provide atomistic information on the local crystal structure of the cathode before and after electrochemical operations. The high precision of TEM would not only aid in validating the results of the XRD measurements but also in detecting defects (disorders) outside the detectable limit of XRD measurements.

Herein, in an attempt to shed light on the structural nature and topological behaviour of the enigmatic P-type honeycomb structures, we utilise atomic-resolution scanning transmission electron microscopy (STEM) to explicitly reveal structural disorders of honeycomb layers along *c*-axis in pristine $K_2Ni_2TeO_6$ cathode material. The analyses reveal partially missing honeycomb slabs of NiO_6 and TeO_6 octahedra as well as the absence of some constituent K atoms, creating unique topological defects and curvatures within the pristine material. Furthermore, we find both P2- and P3-type stacking sequences, whereby the occurrence of the topological defects and curvature is correlated with missing atoms (dislocations) and the appearance of the P3-type stacking. Since (de)intercalation processes are known to trigger transitions between stacking sequences during battery operation, this evidence provides a segue into understanding phase transitions in honeycomb layered oxide frameworks solely through the study of such defects and curvature.

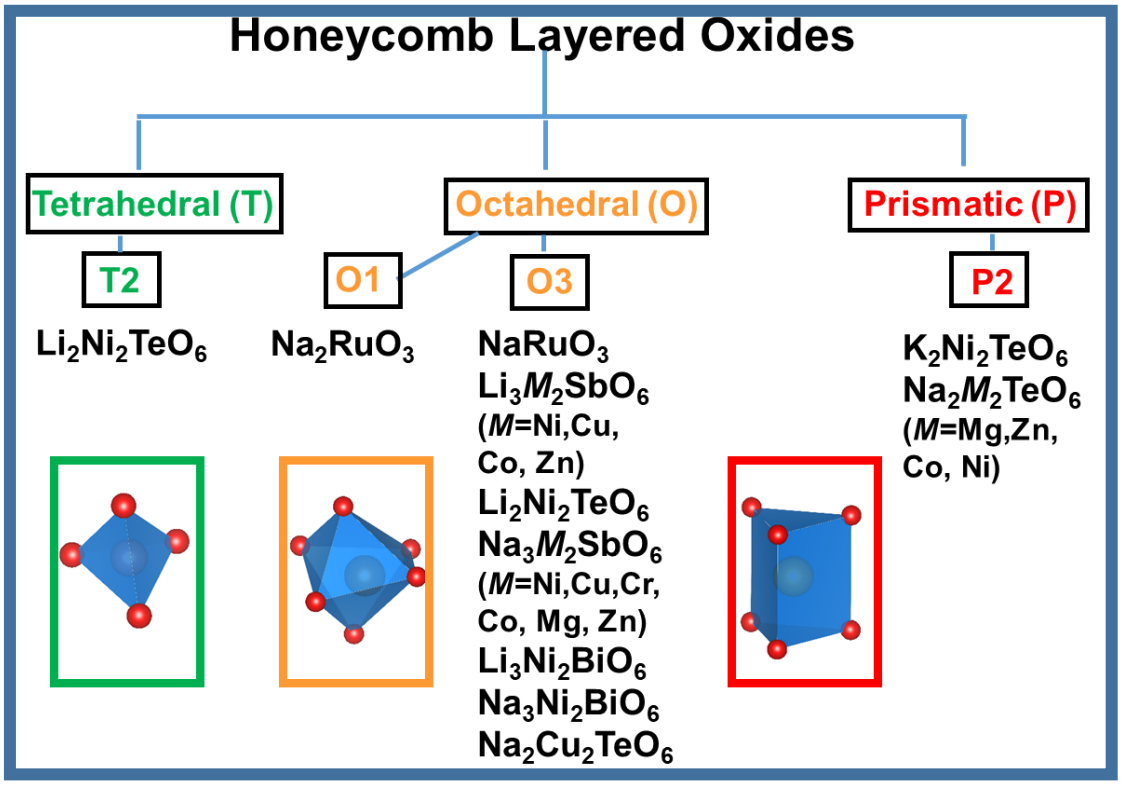

Fig. 1. Layer stackings and the nature of alkali-atom coordination adopted by representative honeycomb layered oxides. Summary of the major stacking sequences adopted by representative honeycomb layered oxides reported so far. [5, 8, 11, 15, 31, 37–54] Note here that T, O and P denote the coordination of the alkali atoms (sandwiched between the honeycomb slabs) with the adjacent oxygen atoms of the honeycomb slab. In this case, the letters 'T', 'O' and 'P' denote tetrahedral (highlighted in green), octahedral (in orange) and prismatic (in red) coordination, respectively. Moreover, the numbers '1', '2' and '3' respectively indicate that the coordinated honeycomb have a consistent stacking sequence with a period of one, two and three layers.

RESULTS

MATERIAL CHARACTERISATION

Polycrystalline samples of $K_2Ni_2TeO_6$ were synthesised through the conventional high-temperature solid-state ceramics route (see details provided in the **METHODS** section). X-ray diffraction (XRD) analyses unambiguously reveal the pristine $K_2Ni_2TeO_6$ to be indexable to the hexagonal lattice adopting the centrosymmetric $P6_3/mcm$ space group as the average structure, [8] as explicated in **Supplementary Fig. 1** and **Supplementary Table 1**. In addition, inductively coupled plasma-atomic emission spectroscopy (ICP-AES) analysis shows the atomic ratio Te / Ni ≈ 0.5 and (Ni + Te) / K ≈ 1.5, in line with the proprietary composition $K_2Ni_2TeO_6$ (see **Supplementary Table 2**). Scanning electron microscopy (SEM) was conducted in order to investigate the grain size and morphology of the pristine $K_2Ni_2TeO_6$ samples, revealing a uniform micrometric-size particle distribution (shown in **Supplementary Fig. 2**). In addition, flake-like (lamellar-like) grain shapes are evident which is typically seen in layered oxides such as K_xMnO_2.[56] **Figure 2a** shows the layered crystal framework of $K_2Ni_2TeO_6$ along the *a*-axis ([100] zone axis) as deduced from the XRD analyses shown in in **Supplementary Fig. 1** and **Table 1**.

The synthesised $K_2Ni_2TeO_6$ displays a layered crystal structure comprising K atoms coordinated with oxygen atoms interposed between slabs of NiO_6 and TeO_6 as illustrated by **Fig. 2a.** The NiO_6 slab is composed of nickel atoms coordinated to six oxygen atoms, whereas the TeO_6 contains Te atoms also coordinated to six oxygen atoms. As shown in **Fig. 2b,** a honeycomb configuration of NiO_6 and TeO_6 octahedra is formed with each TeO_6 surrounded by six NiO_6 octahedra. This is as a result of the hexavalent state and the divalent state of $Te^{6+}$and Ni^{2+} respectively (see **Supplementary Fig. 3**). The resulting layered structure of $K_2Ni_2TeO_6$ further reveals a prismatic coordination of the K atoms with two repetitive layers of NiO_6 and TeO_6 octahedra in the unit cell, confirming $K_2Ni_2TeO_6$ as a P2-type structure.[36]

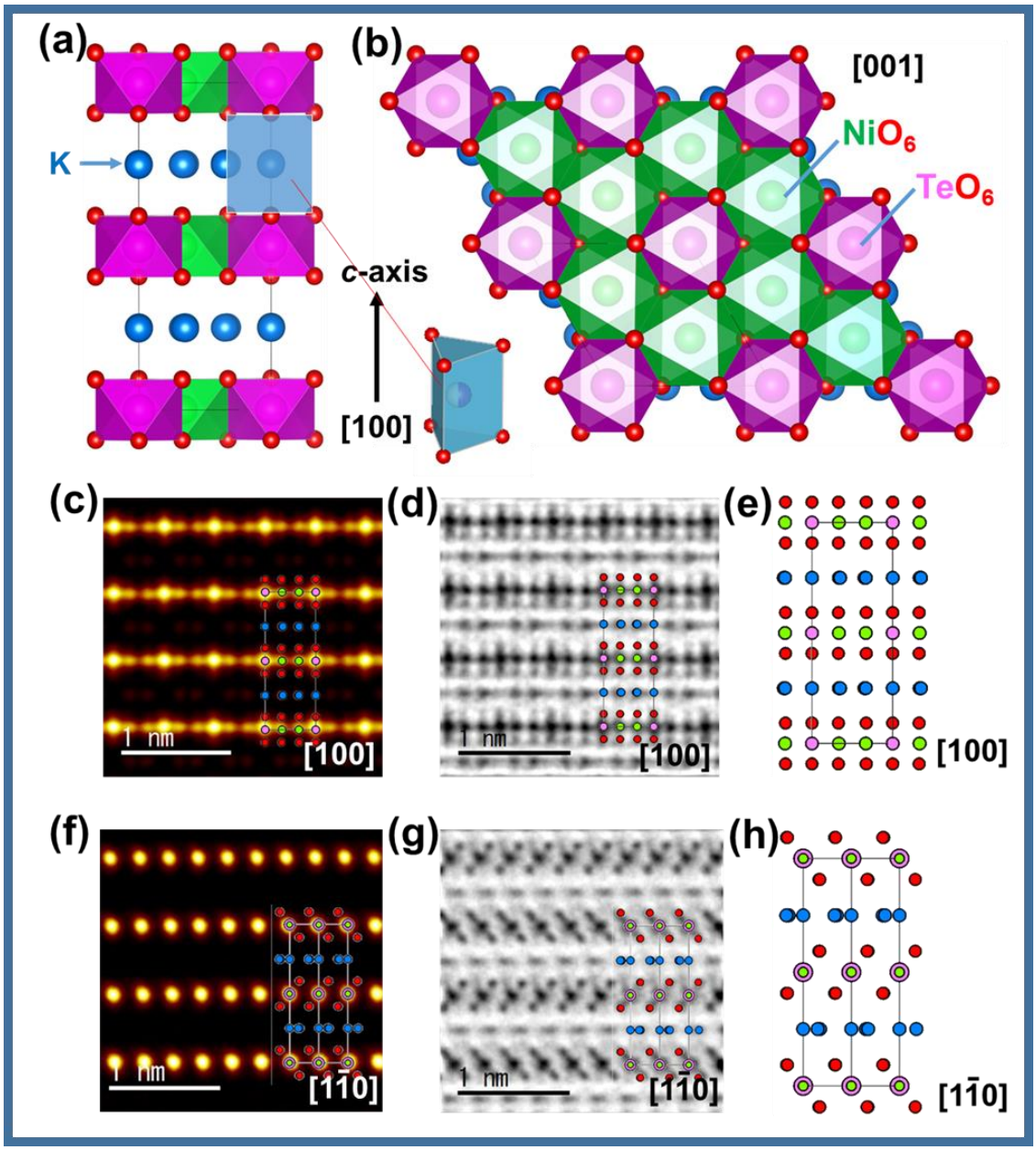

Fig. 2. Visualisation of the honeycomb configuration of metal atoms in P2-type $K_2Ni_2TeO_6$ along the *c*-axis. a Crystal structure of $K_2Ni_2TeO_6$ along [100] projection showing the P2-type coordination (prismatic coordination of the K atoms and 2 honeycomb slab layers in the unit cell (shown in black). Throughout the figures K atoms are shown in blue, Te in pink, Ni in green, and O in red. **b** Projection along [001] showing the honeycomb arrangement of Ni atoms around Te atoms. **c** High-angle annular dark-field scanning transmission electron microscopy (HAADF-STEM) image taken along [100] zone axis showing the ordering sequence of Ni and Te atoms corresponding to the P2-type stacking. Inset shows an atomistic view of the crystal structure, for clarity. **d** Annular bright-field (ABF)-STEM image along [100] zone axis

showing also the arrangement of potassium atoms. **e** Rendering of the P2-type stacking of $K_2Ni_2TeO_6$ along the [100] direction. **f** Visualisation (along the [1-10] zone axis) using HAADF-STEM, and **g** ABF-STEM. **h** Projection of the crystal structure along [1-10], affirming the polyhedral representation of P2-type stacking of atoms as shown in **f** and **g**.

TYPICAL P2-TYPE STACKING OF ATOMS

In order to attain information pertaining to the honeycomb ordering and slab stacking sequence of the synthesised $K_2Ni_2TeO_6$, aberration-corrected scanning transmission electron microscopy (STEM) was employed. Considering that prolonged electron beam irradiation gradually leads to sample degradation (as can be seen in **Supplementary Fig. 4**), the short-time exposure of the sample to electron beams was sufficient to obtain reliable high-resolution TEM (HRTEM) imaging without compromising the stability of the honeycomb layered structure (see more details in the **Supplementary Information** section). **Figure 2c** explicitly shows atomic-resolution high-angle annular dark-field scanning TEM (HAADF-STEM) images of the P2-type stacking of $K_2Ni_2TeO_6$ as viewed in the [100] zone axis. For clarity, the contrast (I) of the STEM images are proportional to the atomic number (Z) of elements along the atomic arrangement (where $I \propto Z^{1.7} \approx Z^2$). [57–59] The brighter and bigger yellow spots correspond to Te atoms (Z = 52), whilst the smaller yellow spots represent Ni atoms (Z = 28). When viewed in the [100] zone axis projection, the Te–Ni–Ni–Te sequence along the b-axis is apparent, as expected for a perfectly ordered P2-type honeycomb stacking sequence illustrated by the crystal structure model (**Fig. 2c**). The arrangement of the constituent atoms of $K_2Ni_2TeO_6$ is further validated by atomic-resolution elemental mapping, taken along the [100] zone axis (**Supplementary Fig. 5**). Close inspection using annular bright-field (ABF)-STEM, as shown in **Fig. 2d**, shows K atoms (Z = 19) positioned between the NiO_6 and TeO_6 slabs in a sandwich-like arrangement. HAADF- and ABF-STEM images taken along the [1-10] zone axis (**Figs. 2f** and **2g**) further affirm the arrangement of K atoms, seen to be occupying crystallographically distinct sites with varying occupancies (see **Supplementary Table 1**), as can also be identified by the differing contrasts of K atoms shown in **Fig. 2d**. As illustrated in **Fig. 2h**, the crystal model of the P2-type $K_2Ni_2TeO_6$ viewed along the [1-10] zone axis further corroborates the assignment of atoms in the HAADF-STEM and ABF-STEM images shown in **Figs. 2f** and **2g**, respectively.

In well-reported honeycomb layered oxide structures such as $Na_3Ni_2SbO_6$, a defect

chemistry involving the cationic mixing of transition metals where Ni and Sb swap their crystallographic site positions has been observed.[60] To ascertain whether cationic mixing behaviour exists in $K_2Ni_2TeO_6$, HAADF-STEM images of the cathode material viewed along the [001] zone axis were obtained as shown in **Fig. 3a**. To reiterate, the Ni atoms are depicted by the dark red spots whilst the brighter yellow spots indicate the Te atoms. The corresponding ABF-STEM images (**Fig. 3b**) explicitly confirm the honeycomb configuration of Ni atoms

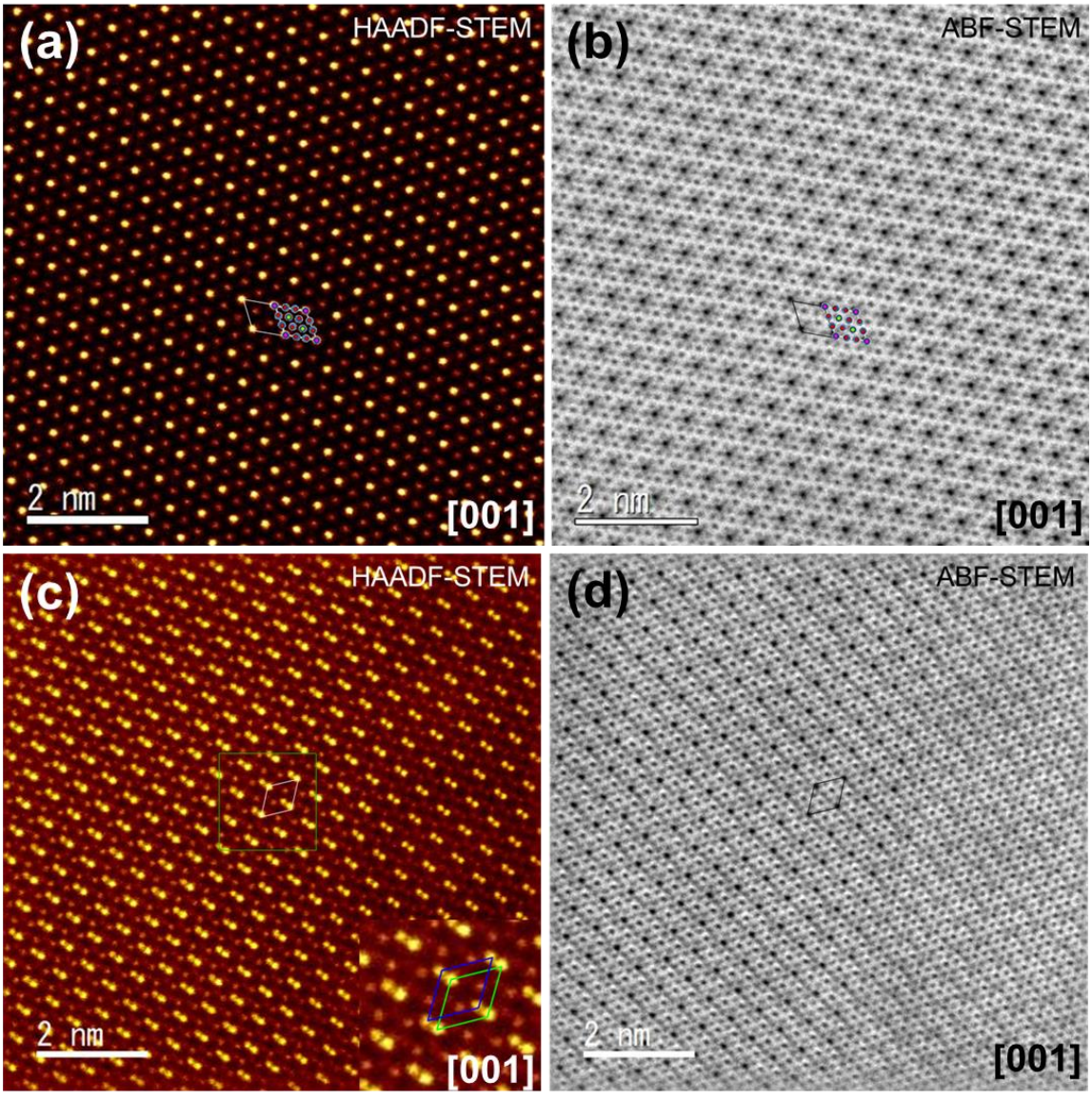

Fig. 3. Visualisation of the honeycomb configuration of metal atoms in P2-type $K_2Ni_2TeO_6$ along the *c*-axis. a HAADF-STEM images along the [001] zone axis showing an ordered honeycomb arrangement of Ni (dark red spots) around the Te atoms (shown as bright yellow spots). Inset shows a polyhedral atomic view of the crystal

structure, for clarity to the readers. **b** Corresponding ABF-STEM images along the [001] zone axis showing the atomic arrangement of Ni and Te atoms, in addition to atoms of lighter atomic mass such as potassium. **c** HAADF-STEM image taken along the [001] zone axis for a honeycomb slab part that shows doublets of both bright and dark spots (as shown further in inset), indicative of shearing (sliding) of the honeycomb slab (hence, the existence of stacking faults) along the *ab* plane with a slab-to-slab translation vector of [1/3 1/3 0]. **d** Corresponding ABF-STEM micrographs taken along the [001] zone axis.

around Te atoms alongside K atoms overlapping with oxygen atoms (Z = 8). Cationic mixing between transition metal Ni and Te sites was not detected in the various crystallites investigated. This observation is not unprecedented, as the Shannon-Prewitt ionic radius of Te^{6+} in octahedral coordination (0.56 Å) is relatively smaller than that of Ni^{2+} (0.69 Å). [61] Despite the difference in ionic radius, a recent study has reported the existence of infinitesimal cationic mixing disorders between Te^{6+} (0.56 Å) and Zn^{2+} (0.74 Å) octahedra in the O3-type $Na_2Zn_2TeO_6$.[62] Thus, the existence of Ni / Te antisite mixing cannot be completely ruled out in the case of $K_2Ni_2TeO_6$. Nevertheless, within the detectable limits of TEM, the absence of Ni and Te cationic site mixing substantiates XRD analyses that show full occupancy of Ni and Te sites not only in $K_2Ni_2TeO_6$ (**Supplementary Table 1**), but also in related tellurates.[4–6, 8, 39, 41, 42, 63] The honeycomb arrangement of the Te and Ni atoms is also seen upon closer inspection of $K_2Ni_2TeO_6$ particles through atomic-resolution elemental mapping, taken along the [001] zone axis (**Supplementary Fig. 6**). Crystallite domains with doublets of Te and Ni spots appear to form a peculiar diagonal-like pattern among some particles of $K_2Ni_2TeO_6$ as shown in **Figs. 3c** and **3d**. The enlarged STEM image in **Fig. 3c** clearly shows that, in these domains, adjacent honeycomb slabs deviate from the perfect vertical alignment of Te and Ni atoms (**Figs. 2e** and **2h**) along the [100] and [1-10] zone axes. Based on the slab stacking sequence along the *c*-axis ([001] direction), the adjacent slab shifts (by a translation vector we determined to be [1/3 1/3 0]) suggest that the new stacking variant in pristine $K_2Ni_2TeO_6$ material may best be observed along the *a*-axis ([100]) or *b*-axis ([010]).

NEW P3-TYPE STACKING OF ATOMS

Therefore, for a closer probe into the new stacking variants, HAADF-STEM and ABF-STEM images of $K_2Ni_2TeO_6$ were taken along the [100] zone axis, as can be seen in **Figs. 4a** and **4b.** The initial P2-type slab stacking (shown in green line) can be

observed as well as a new slab stacking domain that appears to shift along the *b*-axis.

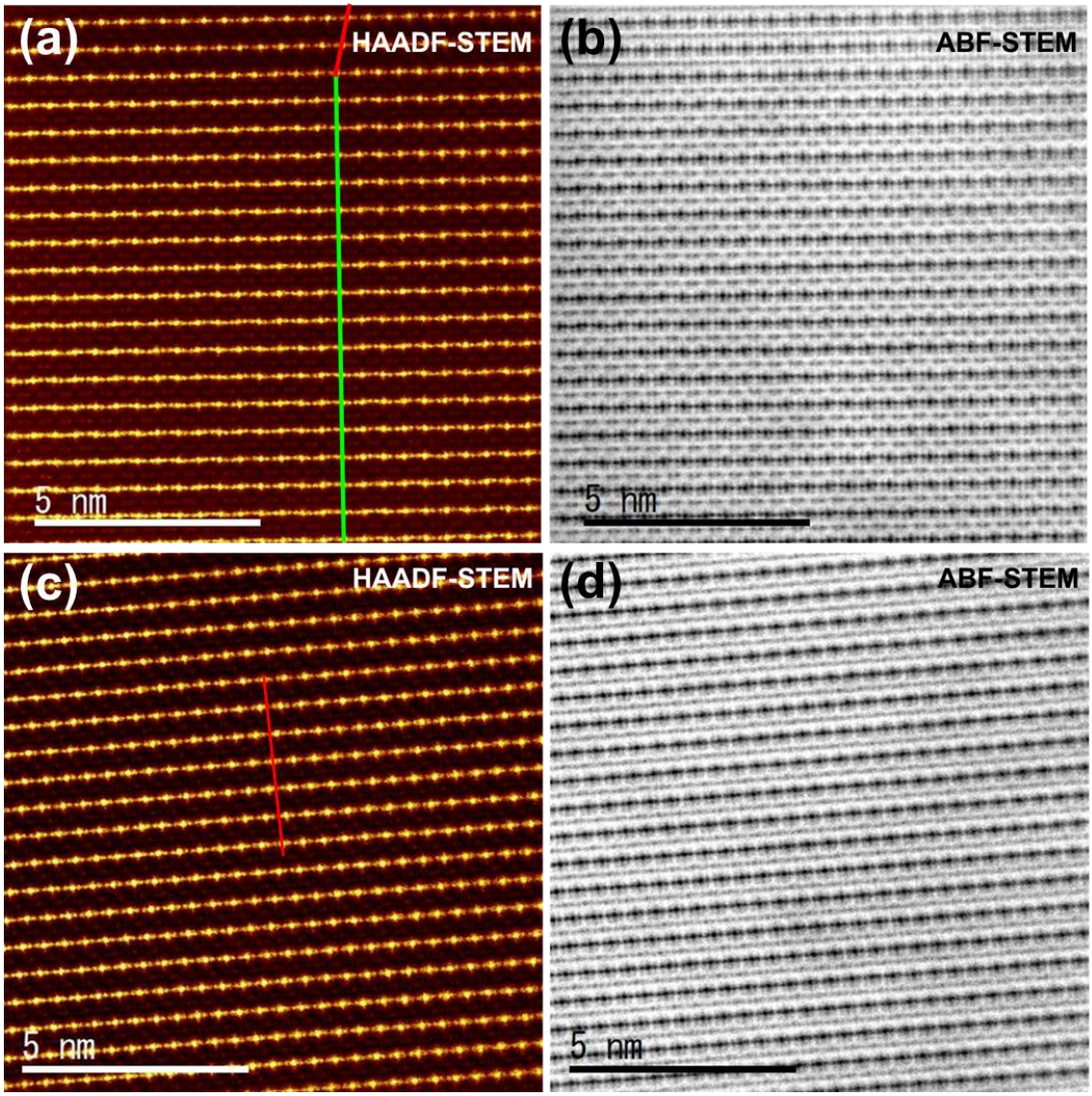

Fig. 4. Identification of a new stacking sequence (P3-type) in $K_2Ni_2TeO_6$ along the *a*-axis. a HAADF-STEM image taken along the [100] zone axis showing a new type of stacking (arrangement of which is shown in red line) that is distinct from the P2-type stacking (shown in green line). **b** Corresponding ABF-STEM images showing the arrangement of potassium atoms between the honeycomb slabs along the [100] zone axis. **c** HAADF-STEM micrographs of the domains adopting the new P3-type stacking along the [100] direction. The red line is a guide to the eye. **d** Corresponding ABF-STEM images taken along the [100] zone axis showing the arrangement of potassium atoms sandwiched between the P3-type stacking of honeycomb metal slabs.

More details into the new slab stacking is furnished in the HAADF-STEM images

shown in **Fig. 4c** showing the arrangement of Te atoms to be repeatable after three K layers along the *c*-axis (inset). The arrangement of the new stacking domain *vis-a-vis* the occupancy of the potassium atoms coordinated with oxygen atoms can clearly be observed through the corresponding ABF-STEM images (**Fig. 4d**).

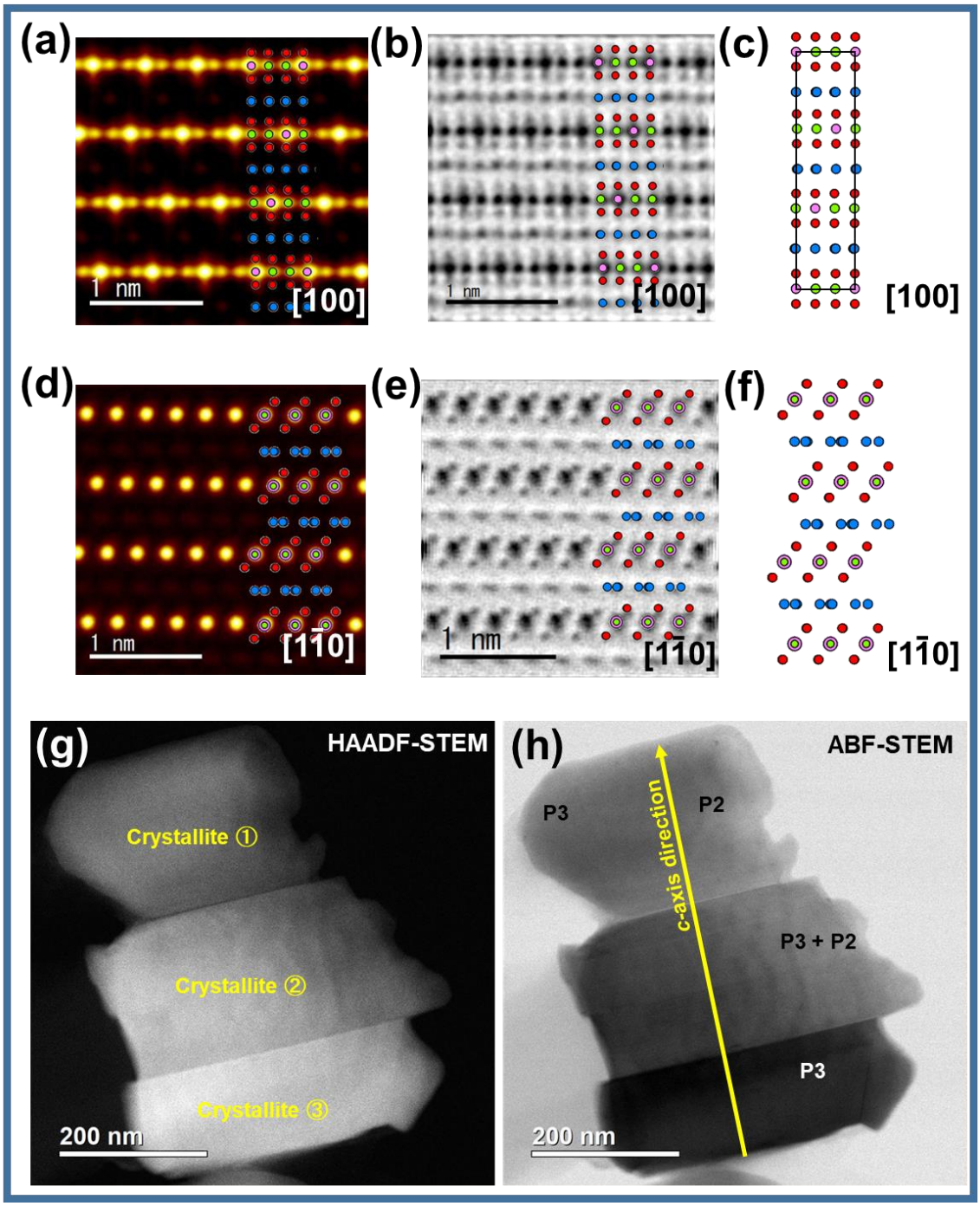

Fig. 5. The newly identified P3-type stacking sequence in $K_2Ni_2TeO_6$. a Typical HAADF-STEM image taken along [100] zone axis showing the ordering sequence of Ni and Te atoms corresponding to the P3-type stacking. Inset shows an atomistic

depiction of the crystal structure, for the sake of clarity. **b** Corresponding ABF-STEM images taken along [100] zone axis showing also the arrangement of potassium atoms. **c** Representation of the crystal structural framework of P3-type $K_2Ni_2TeO_6$ along the [100] direction. **d** Visualisation (along the [1-10] zone axis) using HAADF-STEM, and **e** ABF-STEM. **f** Projection of the crystal structure along [1-10], affirming the polyhedral representation of P3-type stacking of atoms as shown in **d** and **e**. **g** Low magnification HAADF-STEM micrographs of a section of crystallites aligned in various zone axes, as revealed by the varying degree of contrasts. **h** Corresponding ABF-STEM images showing crystallites with entirely P3-type stackings and some with a mixture of both P2-type and P3-type stackings. Details relating to the acquisition of the magnified images are furnished in the **Supplementary Information** section.

To further assess the nature adopted by the new stacking, atomic-resolution HAADF-STEM and ABF-STEM images were taken as shown in **Figs. 5a** and **5b**. A new P3-type stacking is noted to have been formed by the slab-to-slab transition vector [1/3 1/3 0] relative to the main crystallographic axes. Thus, a new sequence with Te–Ni–Ni–Te alternating along the *c*-axis is formed, as displayed in the crystal model shown in **Fig. 5c**. To further verify the atomic arrangements in this P3-stacking sequence along multiple zone axes, STEM images were also taken along the [1-10] zone axis, as shown in **Figs. 5d** and **5e**. The projected crystal structural model along the [1-10] is shown in **Fig. 5f**. It is worth noting that the occupancy of K atoms in the various crystallographic sites of this new P3 stacking is different, as indicated by the varying contrasts of the K atom coordinated with oxygen atoms along wavy-like columns in the *ab* plane as illustrated by the projected structure model in **Fig. 5c**. Similarly, the occupancy of potassium atoms with respect to the position of oxygen atoms can be ascertained from the ABF-STEM images. By locating the position of oxygen atoms along [1-10] zone axis, the salient atomic structural differences between P2- and P3-type frameworks can be distinguished. The oxygen atoms are arranged diagonally in a zig-zag orientation along the *c*-axis in the P2-type framework (see **Fig. 2g**), whilst for the P3-type variant framework the oxygen atoms are aligned in the same direction on the *ab* plane (**Fig. 5e**). These emergent P3-type stackings could also be discovered in the low-magnification STEM images (**Figs. 5g** and **5h**), where crystallites dominant with P3-type stacking were seen adjacent to previously reported P2-type stackings. These observations not only demonstrate the emergence of a new type of stacking (P3-type) in pristine $K_2Ni_2TeO_6$, but also explicitly point to the existence of stacking variants (faults or disorders). Even so, an extensive examination into their

stacking sequences is still necessary in order to garner a deeper insight into their crystallographic information.

As such, selected area electron diffraction (SAED) measurements were duly performed, exhibiting patterns of a crystallite with P2-stacking sequence along the [1-10] and [100] zone axes, as shown in **Figs. 6a** and **6c**. The corresponding simulations are shown in **Figs. 6b** and **6d**, revealing a good match with the experimental diffractograms indexable to the hexagonal lattice of the P2-type phase. For comparison, the SAED patterns of a crystallite with P3-type stacking sequence are provided in **Figs. 6e** and **6g** along with their corresponding simulations (**Figs. 6f** and **6h**). The patterns of the domain with the P3-type stacking along [1-10] and [010] zone axes (**Figs. 6e** and **6g**), reveal arrays of pseudo-hexagonal symmetry dots that could be indexed into a slightly-distorted hexagonal cell with the approximate lattice parameters: $a \approx 5.26$ Å, $c \approx 18.70$ Å (interslab distance of 6.23 Å). The P3-type lattice parameters are very close to the lattice parameters obtained from the P2-type stacking: $a \approx 5.25$ Å, $c \approx 12.44$ Å (interslab distance of 6.22 Å). Indeed, this explains why this new stacking (P3-type) variant was undetected by the low precision bulk XRD analyses as its crystallite concentration is presumably rather subtle to be sufficiently distinguished. A further inspection of the electron diffractograms of P3-type stacking (**Figs. 6e** and **6g**) indicate angle deviations 77.7^0 and 82^0 from the adjacent main diffraction spots along the [1-10] and [010] zone axes, respectively. Typically, angle deviations are expected to fall around 90^0 with an accuracy range *ca.* 1% as such errors arising from experimental flaws can be ruled out from the inclinations observed in the electron diffractograms. Based on the extinction conditions, the SAED patterns of the P3-type stacking are indexable to a triclinic *P*-1 space group. Furthermore, the ordering of P3-type stacking sequence is formed by a slab-to-slab translation vector [1/3 1/3 0] relative to the main crystallographic axes of P2-type stacking, concomitant with distortions that slightly alter the inclination angle of the main axes.

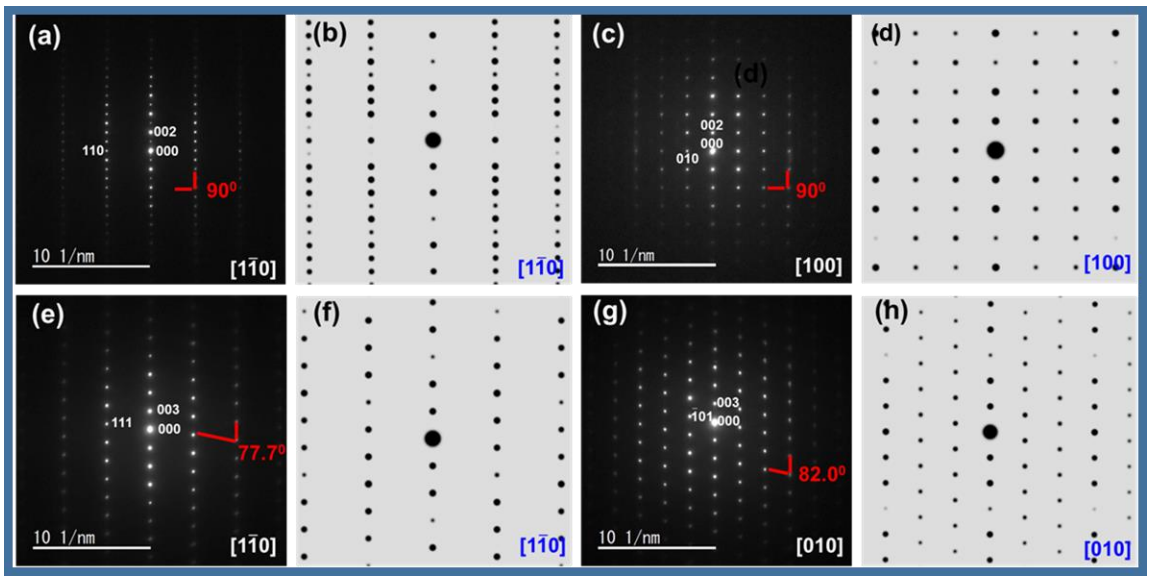

Fig. 6. Comparison of the electron diffraction patterns of P2- and P3-type $K_2Ni_2TeO_6$. Selected area electron diffraction (SAED) images of P2-type stacking along **a** [1-10] zone axis and **b** corresponding simulation. **c** SAED images of P2-type stacking taken along [100] and **d** corresponding simulation. **e** SAED images of P3-type stacking taken along the [1-10] zone axis and **f** corresponding simulation. **g** SAED images of P3-type stacking taken along the [010] zone axis and **h** the corresponding simulation.

TOPOLOGICAL DEFECTS (DISLOCATION STRUCTURES) IN $K_2Ni_2TeO_6$

Motivated by the existence of stacking variants in the pristine $K_2Ni_2TeO_6$, further attempts to look at other defects were made. Unexpectedly, structural defects related to imperfections that culminate in the disappearance or bending of the honeycomb slabs and potassium layers were captured *for the first-time*. **Figures 7a** and **7b** show low-magnification STEM images of crystallite domains with P3-type stacking slab sequence. At first glance, it seems that grain boundary lines separate various crystallites oriented in different zone axes. However, a closer inspection, more specifically using atomic-resolution HAADF-STEM images (**Fig. 7c**), reveal the warping or bending of the honeycomb slabs. Corresponding ABF-STEM images of these regions (**Fig. 7d**) further show similar warping on the potassium layers that may be mistaken for twin or tilt boundaries. Moreover, defects that relate to curvature of the honeycomb slab surface can also be discerned from the high-magnification STEM images (**Figs. 7e** and **7f**) that show an undulating topology of both the honeycomb slabs and potassium layers along the *b*-axis. Such defects are exceedingly rare in layered oxides, which spurred our

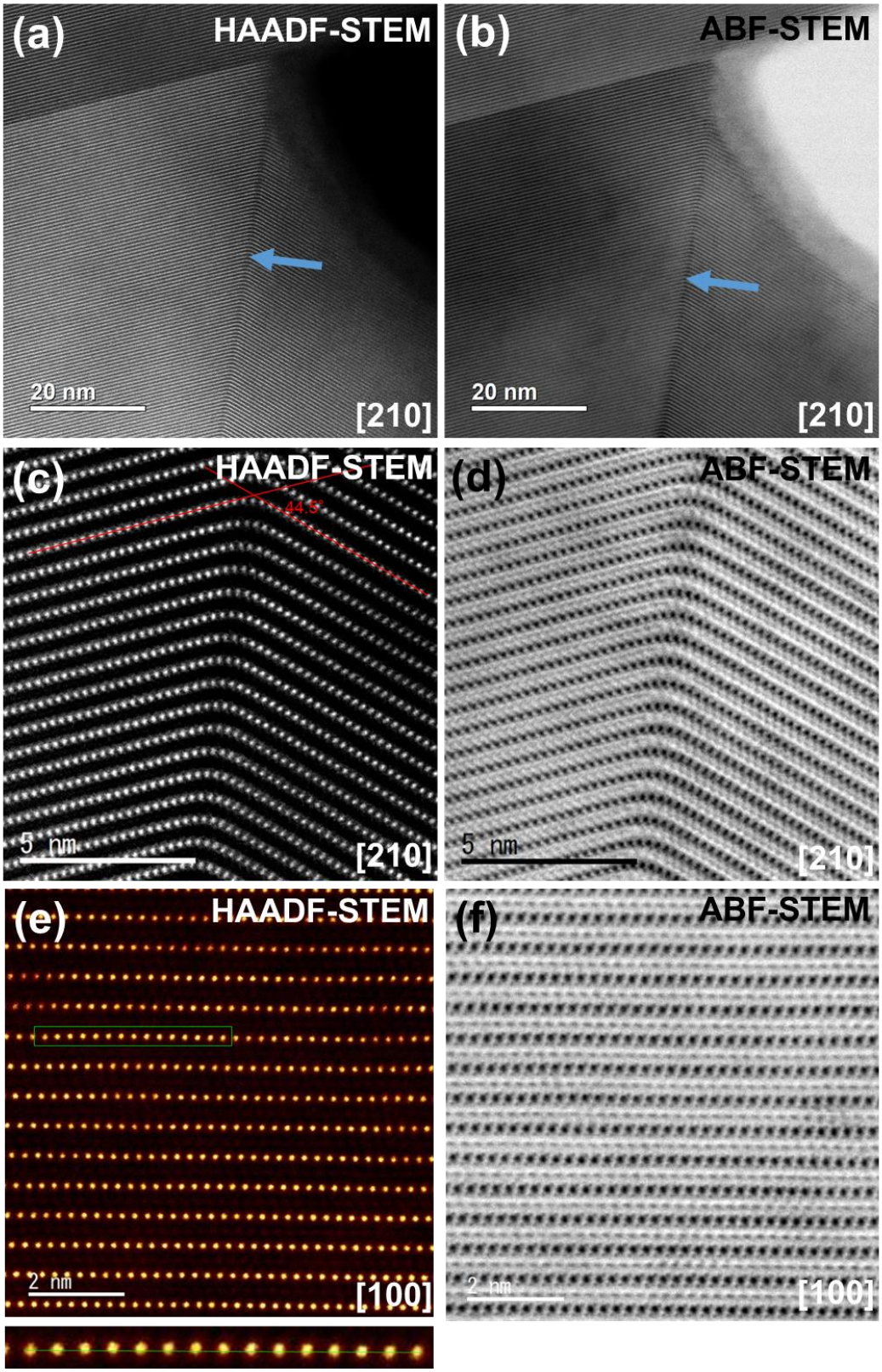

Fig. 7. Topological defects related to strong curvature in P3-type $K_2Ni_2TeO_6$. a, b High resolution TEM micrographs of a section of P3-type stacking that shows curvature

defects along [210] zone axis (underpinned using arrows). **c** HAADF-STEM images along [210] zone axis showing the bending of the honeycomb slab layer at an angle of 44.5^0 relative to the horizontal planes (as highlighted in red) and **d** Corresponding ABF-STEM images showing the bending of the alkali atoms layer (in this case, potassium). **e** HAADF-STEM images taken along [100] direction showing the undulating nature of the honeycomb metal stabs (as highlighted in inset (green line)) and **f** Corresponding ABF-STEM images also showing the undulating nature of the potassium atom layers across the honeycomb slab surface.

interest to further investigate the defects in the honeycomb layered framework of $K_2Ni_2TeO_6$.

Topological defects such as (Taylor's) dislocations and disclinations, where translational and rotational symmetry respectively of the atoms in the crystal is destroyed, are gaining traction these days as they play host to distinct physicochemical properties. [64] Moreover, such symmetry violations in the crystal can profoundly affect the dynamics of alkali cations during (de)intercalation processes for crystalline symmetries are intricately linked with momentum and angular momentum conservation laws. [65] **Figure 8a** shows a HAADF-STEM image of a lattice domain adopting a P2-type stacking along the [100] zone axis, where a curvature appears as a result of part of the honeycomb slab laying out of position. In essence, dislocations are induced in the crystal lattice, whose origin (technically, dislocation core) is denoted by the symbol 'T' (highlighted in **Fig. 8a**). The corresponding ABF-STEM images reveal considerable distortions on the $K_2Ni_2TeO_6$ lattice as shown in **Fig. 8b.** More details relating to the edge dislocations can be observed from the HAADF-STEM and ABF-STEM images shown in **Figs. 8c** and **8d** respectively. The images indicate that these dislocations are created by a shift along the a*b*-plane with a translation vector [1/3 1/3 0]. In principle, the magnitude and direction of the lattice distortion arising from the edge dislocation can be represented using a Burgers vector (***b***). The Burgers vector of the edge dislocation imaged in **Figs. 8a** and **8b** was determined to be [0 1 0], spanning along the *b*-axis (slip plane). As for the edge dislocations appearing in **Fig. 8c** and **8d**, the Burgers vector was determined to be [1/3 1/3 1/2] which spans along the *b*-axis. Other unique edge dislocations detected during the analysis were determined to shift with a Burgers vector of [–1/3 –1/3 1/2] as indicated in **Supplementary Fig. 7**. It is important to note that despite proving elusive to ascertain, other shifts occurring along the *a*-axis cannot be ruled out. It must also be noted that the varied and capricious nature of the edge dislocations observed in our

investigation are unique to P3-type structures and are extremely rare amongst oxides.

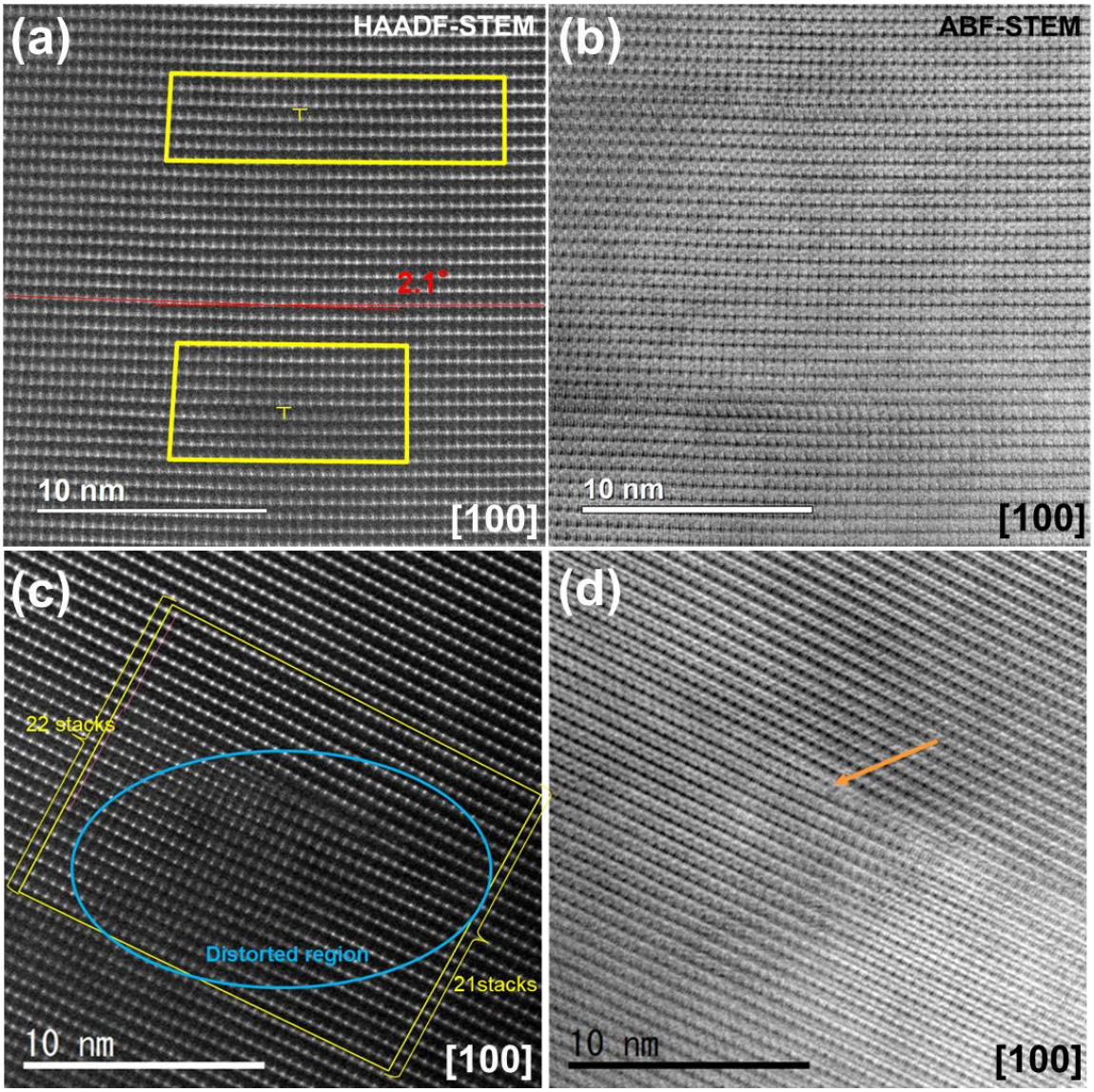

Fig. 8. **Topological defects related to weak curvature in P2-type $K_2Ni_2TeO_6$.** **a** HAADF-STEM images of P2-type stacking along the [100] zone axis, showing the bending of the honeycomb slabs owing to the formation of defects (in particular, edge dislocations). The point of origin of the dislocation is shown as 'T'. For clarity, the 'T' shape labels the slab mismatch direction in the edge dislocation core. **b** Corresponding ABF-STEM images along the [100] zone axis also showing the bending of the potassium atom layers. **c** HAADF-STEM images of a distorted honeycomb slab section of the P2-type stacking along the [100] zone axis and **d** the corresponding ABF-STEM images along the [100] zone axis highlighting the distorted slab where edge dislocations have occurred (highlighted by an arrow).

DISCUSSION

Through this study, we not only discover the perturbation of the P2-type slab stacking sequence of honeycomb layered oxide $K_2Ni_2TeO_6$, but also unearth the existence of topological defects such as dislocations and curvature. Whilst the vast majority of pristine honeycomb layered oxides adopt the O3-type (see **Fig. 1**), by employing the atomic-resolution of TEM on $K_2Ni_2TeO_6$ a new P3-type stacking sequence is revealed alongside previously reported P2-type stacking, (as is furnished in **Fig. 9**) additionally augmenting the database for the stacking sequences of honeycomb layered oxides.

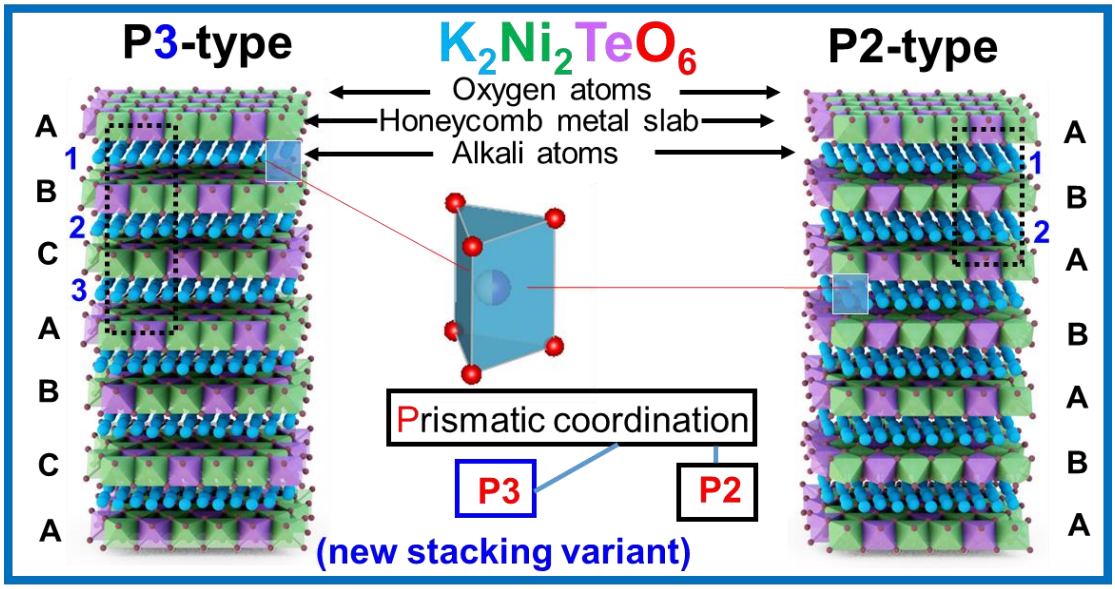

Fig. 9. Honeycomb slab stacking arrangement found in pristine $K_2Ni_2TeO_6$. Stacking sequence of honeycomb slabs and K atoms in P2-type (**ABABABA**…stacking of oxygen atom slab) and P3-type (**ABCABCA**…) $K_2Ni_2TeO_6$, as revealed by TEM. Honeycomb slabs comprising Ni and Te are shown in green, oxygen in red whilst K in blue. The numbers (1, 2 and 3) indicate the repetitive potassium layers per unit cell.

As explicated earlier (in the **INTRODUCTION** section), amongst honeycomb layered oxides, P3-type stackings have only been observed as intermittent products of electrochemical reactions during the (de)insertion of alkali ions during battery operations. [15, 55] Herein, we observe *for the first time*, P3-type stacking variants alongside P2-type stacking sequences in $K_2Ni_2TeO_6$ crystallites as shown in **Supplementary Figs. 5g** and **5h**. Although these stackings have almost similar interslab distances (*i.e.* 6.22Å and 6.23Å for P2-type and P3-type respectively), P3-type adopts a sequence whereby every honeycomb slab unit of P2-type sequence shifts from each

adjacent slab unit by a vector of [1/3, 1/3, 0]. Such a mixture of stacking sequences (**ABABABA**… *versus* **ABCABCA**… (as succinctly shown in **Fig. 9**)) can induce partial dislocations, as observed in this study.

Dislocations in oxides constitute a vast swath of topological defects which are associated with intriguing physicochemical properties. For example, dislocation structures in ternary oxides such as $SrTiO_3$ display resistive-switching behaviour, ferromagnetic dislocations have been observed in antiferromagnetic NiO and non-superconducting dislocation cores have been shown to act as pinning centers for magnetic flux lines in some classes of superconductors. [64] In addition, dislocations that occur upon Li^+ (de)insertion in layered oxides such as the exemplar $LiCoO_2$, and more recently, $Li_{1.2}Ni_{0.133}Mn_{0.533}Co_{0.133}O_2$ influence the voltage output characteristics, [66–68] indicating the role of dislocations in tuneable electrochemistry of energy materials where honeycomb layered oxides such as $K_2Ni_2TeO_6$ will generate immense utility as high-voltage battery materials.

The identification of topological defects in $K_2Ni_2TeO_6$ such as edge dislocations (**Fig. 8**) and curvature (**Fig. 7**) may provide crucial information to understand the transport (diffusion) mechanism of K^+, for instance, during operation as battery cathode materials. In fact, in a previous work, it has been theorised that there is a direct relation between such curvatures and the vacancy of the cations such as K^+.[65] Particularly, the integral of the curvature (represented as K) over a given patch of area (A) previously occupied by K^+ ions ($\int K dA$) is proportional to the number of cationic vacancies (n) in the given patch area. This is analogous to the well-known formula, Gauss-Bonnet theorem, in two-dimensional geometry relating curvature to topological 'holes' in the layer. [69] These 'holes' act as cationic vacancies forming whenever sufficient activation energy is supplied in the material to offset the binding energy of cations that form the stable P2-lattice, leading to stacking sequence phase transformations such as in the aforementioned $Na_3Ni_2SbO_6$ during Na^+ (de)insertion.[15, 55] Sufficient activation energies can be provided by raising temperatures or by supplying energy-momentum via electrochemical processes within the material.

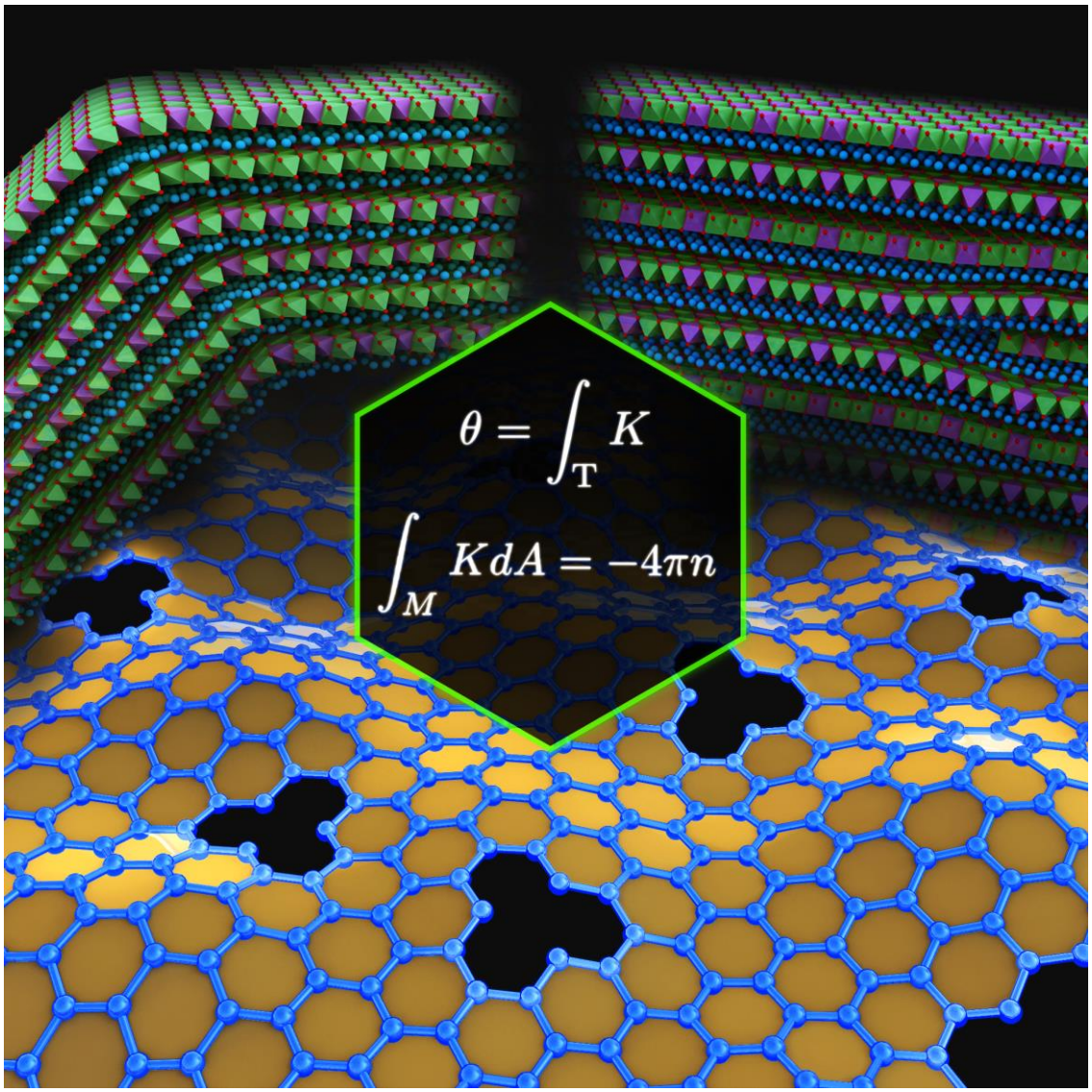

Fig. 10. Implications of the topological defects (2D) and unique stackings (1D). A rendition displaying the honeycomb layer of lithophile cations (shown in blue) in honeycomb layered oxides as curved stacked two-dimensional (2D) manifolds forming a three-dimensional (3D) crystal. The equation $\int_M K\mathrm{d}A = -4\pi n$ links the area (A) integral of Gaussian curvature (K) to the number of cations, n missing from the honeycomb layers responsible for topological defects. Strong curvature can be seen by the bending of the angle $\theta = \int_T K$ over the (geodesic) triangle T traced over the layer. Phase transitions are triggered by these topological defects and can register as unique stackings *e.g.* during alkali-ion (de)intercalation process(es).

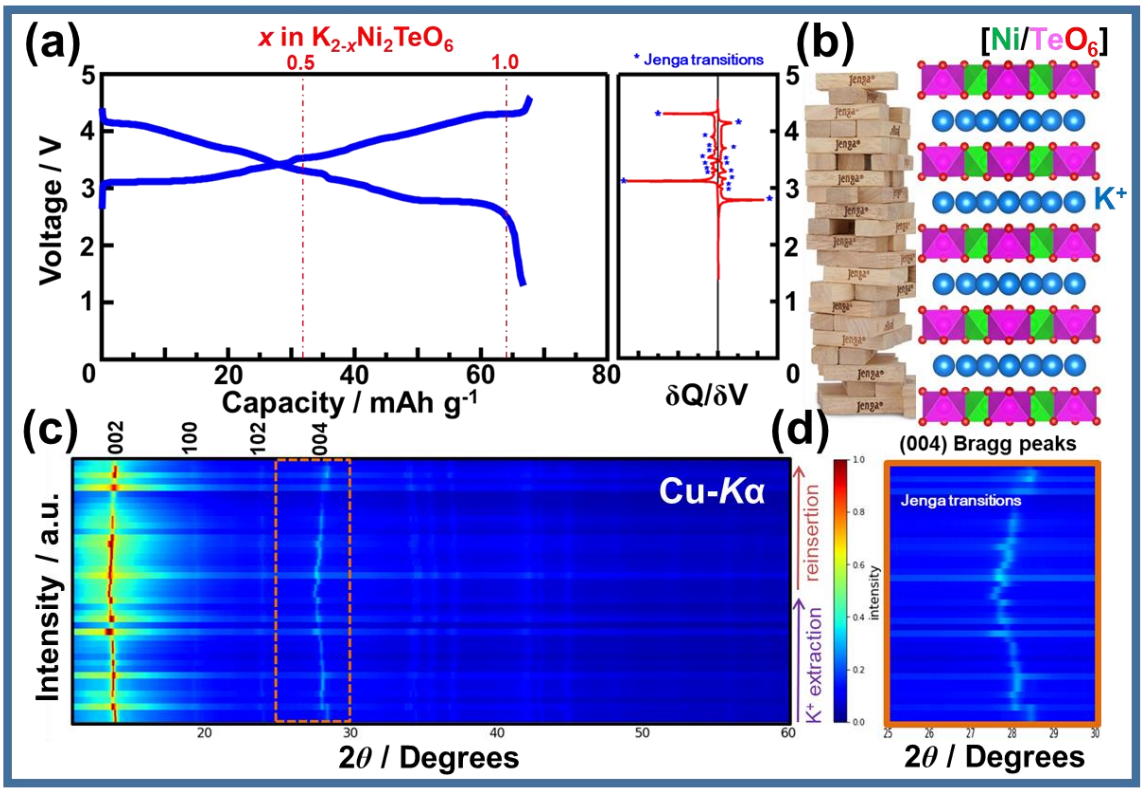

Fig. 11. Understanding topological defects and unique stackings as phase transitions. **a** Initial voltage curves of $K_2Ni_2TeO_6$ depicting staircase-like profiles that are reminiscent of phase transitions as depicted in the derivative capacity-voltage ($\delta Q/\delta v$) curves. **b** Phase transition mechanism in $K_2Ni_2TeO_6$ akin to the process of removing the *Jenga* blocks.[29] **c** X-ray diffraction pattern taken during the (dis)charging process, showing the evolution of the structural changes with K^+ (de)insertion. **d** Enlarged image of the (004) Bragg peaks that are sensitive to K^+ (de)insertion revealing a multitude of phase transitions as revealed from the numerous peak shifts.

A rendition representing such a mechanism is provided in **Fig. 10**. The rendition displays the layers of alkali metal ions such as K^+ in honeycomb layered oxide frameworks as curved stacked two-dimensional (2D) manifolds forming a three-dimensional (3D) crystal. The displayed equation links the curvature variations topological defects as envisioned by the Gauss-Bonnet theorem. [69,*ibid*] The phase transitions are triggered by these topological defects and can register as unique stacking sequences, for instance, during alkali-ion (de)intercalation process(es). [65] **Figure 11** shows such phase transitions triggered during the (dis)charging process and structural evolution during K^+ (de)insertion, experimentally revealed by staircase-like profiles in the derivative capacity-voltage ($\delta Q/\delta v$) curves (**Fig. 11a**) and the observation of a

multitude of Bragg peak shifts (**Figs. 11c** and **11d**), akin to removing stacks of pieces of *Jenga* blocks (*Jenga* mechanism, **Fig. 11b**). [29]

In the case of the $K_2Ni_2TeO_6$ reported in this work, temperatures of above 800 °C were applied during synthesis of these materials, sufficient to offset the binding energies within the stable P2-lattice. Therefore, the phase transition to another stable P-type sequence (P3) in pristine $K_2Ni_2TeO_6$ can possibly be traced to thermally-induced geometric shifts of adjacent honeycomb slabs (shear transformations) and the formation of cationic vacancies during heating, which are accompanied by the topological defects and weak curvatures given in **Fig. 8**. The large ionic radius of K^+ which scales with the interslab distance (hence, weak bonding strength of K with the oxygen atoms in the adjacent honeycomb slabs) also seemingly favours the retention of such topological defects and weak curvature even after adiabatic cool-down, as summarised in **Fig. 7** and **Fig. 8**. HAADF-STEM images along the [210] zone axis in **Fig. 8c** shows that $K_2Ni_2TeO_6$ is extremely malleable even under large stresses which result in even larger curvatures defects.

In conclusion, we utilise aberration-corrected scanning transmission electron microscopy (STEM), which affords a higher-order atomic-resolution, to explicitly reveal structural disorders (variants) of honeycomb layers along *c*-axis in pristine $K_2Ni_2TeO_6$. We find unique topological defects and curvatures due to partially missing honeycomb slabs of NiO_6, TeO_6 octahedra as well as K atoms. Moreover, a new stacking variant with P3-type stacking sequence is for the first time discovered alongside the well reported P2-type stacking domains. In this study, it is postulated that the occurrence of the topological defects and curvature is correlated with missing atoms (dislocations) leading to the emergence of the P3-type stacking. This work further justifies the need for a combination of spectroscopic and imaging techniques to better characterise the nature of such topological defects (both glissile and sessile) incipient in layered oxides. As $K_2Ni_2TeO_6$ finds a niche application as cathode material, electrochemical alkali-ion (de)insertion processes are expected to trigger myriad transitions between stacking sequences. As such, the evidence presented herein also provides a window into understanding phase transitions in honeycomb layered oxide frameworks through the study of such defects and curvature. We expect rekindled interest in the study of the hitherto reported defects and curvature for tuneable electrochemistry not only in honeycomb layered oxides, but also other related layered oxides.

References

1. Zhang, Q. *et al.* Bioinspired engineering of honeycomb structure – Using nature to inspire human innovation. *Prog. Mater. Sci.* **74**, 332–400 (2015).
2. Karihaloo, B. L., Zhang, K. & Wang J. Honeybee combs: how the circular cells transform into rounded hexagons. *J. R. Soc. Interface* **10**, 20130299 (2013).
3. Novoselov, K. S. *et al.* Electric Field Effect in Atomically Thin Carbon Films. *Science* **306**, 666–669 (2004).
4. Sathiya, M. *et al.* Li_4NiTeO_6 as a positive electrode for Li-ion batteries. *Chem. Commun.* **49**, 11376–11378 (2013).
5. Grundish, N. S., Seymour, I. D., Henkelman, G. & Goodenough J. B. Electrochemical Properties of Three $Li_2Ni_2TeO_6$ Structural Polymorphs. *Chem. Mater.* **31**, 9379–9388 (2019).
6. Yang, Z. *et al.* A high-voltage honeycomb-layered Na_4NiTeO_6 as cathode material for Na-ion batteries. *J. Power Sources* **360**, 319–323 (2017).
7. Yuan, D. *et al.* A Honeycomb-Layered $Na_3Ni_2SbO_6$: A High-Rate and Cycle-Stable Cathode for Sodium-Ion Batteries. *Adv. Mater.* **26**, 6301–6306 (2014).
8. Masese, T. *et al.* Rechargeable potassium-ion batteries with honeycomb-layered tellurates as high voltage cathodes and fast potassium-ion conductors. *Nat. Commun.* **9**, 3823 (2018).
9. Bhange, D. S. *et al.* Honeycomb-layer structured $Na_3Ni_2BiO_6$ as a high voltage and long life cathode material for sodium-ion batteries. *J. Mater. Chem. A* **5**, 1300–1310 (2017).
10. Gyabeng, D., Anang, D. A. & Han, J. I. Honeycomb layered oxide $Na_3Ni_2SbO_6$ for high performance pseudocapacitor. *J. Alloys Compd.* **704**, 734–741 (2017).
11. Yadav, D. K., Sethi, A., Shalu & Uma, S. New series of honeycomb ordered oxides, $Na_3M_2SbO_6$ (M(ii) = Mn, Fe, (Mn, Fe), (Mn, Co)): Synthesis, structure and magnetic properties. *Dalt. Trans.* **48**, 8955–8965 (2019).
12. Nalbandyan, V. B., Petrenko, A. A. & Evstigneeva, M. A. Heterovalent substitutions in $Na_2M_2TeO_6$ family: Crystal structure, fast sodium ion conduction and phase transition of $Na_2LiFeTeO_6$. *Solid State Ionics* **233**, 7–11 (2013).
13. Yoshii, K. *et al.* Sulfonylamide-Based Ionic Liquids for High-Voltage Potassium-Ion Batteries with Honeycomb Layered Cathode Oxides. *ChemElectroChem* **6**, 3901 −3910 (2019).

14. Zheng, L. & Obrovac, M. N. Honeycomb Compound $Na_3Ni_2BiO_6$ as Positive Electrode Material in Na Cells. *J. Electrochem. Soc.* **163**, A2362–A2367 (2016).
15. Ma, J. *et al.* Ordered and Disordered Polymorphs of $Na(Ni_{2/3}Sb_{1/3})O_2$: Honeycomb-Ordered Cathodes for Na-Ion Batteries. *Chem. Mater.* **27**, 2387–2399 (2015).
16. Zvereva, E. A. *et al.* A new layered triangular antiferromagnet Li_4FeSbO_6: Spin order, field-induced transitions and anomalous critical behavior. *Dalton Trans.* **42**, 1550–1566 (2013).
17. Sau, K. Influence of ion–ion correlation on Na^+ transport in $Na_2Ni_2TeO_6$: molecular dynamics study. *Ionics (Kiel).* **22**, 2379–2385 (2016).
18. Li, Y. *et al.* A P2-Type Layered Superionic Conductor Ga-Doped $Na_2Zn_2TeO_6$ for All-Solid-State Sodium-Ion Batteries. *Chem. - A Eur. J.* **24**, 1057–1061 (2018).
19. Li, Y. *et al.* New P2-Type Honeycomb-Layered Sodium-Ion Conductor: $Na_2Mg_2TeO_6$. *ACS Appl. Mater. Interfaces* **10**, 15760–15766 (2018).
20. Wu, J. –F., Wang, Q. & Guo, X. Sodium-ion conduction in $Na_2Zn_2TeO_6$ solid electrolytes. *J. Power Sources* **402**, 513–518 (2018).
21. Deng, Z. *et al.* Ca-doped $Na_2Zn_2TeO_6$ layered sodium conductor for all-solid-state sodium-ion batteries. *Electrochim. Acta* **298**, 121–126 (2019).
22. Wu, J. –F., Yu, Z. –Y., Wang, Q. & Guo, X. High performance all-solid-state sodium batteries actualized by polyethylene oxide/ $Na_2Zn_2TeO_6$ composite solid electrolytes. *Energy Storage Mater.* **24**, 467–471 (2020).
23. Dubey, M. *et al.* Structural and ion transport properties of sodium ion conducting Na_2MTeO_6 (M= MgNi and MgZn) solid electrolytes. *Ceram. Int.* **46**, 663–671 (2020).
24. Kee, Y., Dimov, N., Staykov, A. & Okada, S. Insight into Mg-doping effects on $Na_3Ni_2SbO_6$ cathode host for Na-ion batteries. *Mater. Lett.* **183**, 187–190 (2016).
25. Aguesse, F. *et al.* Structural and electrochemical analysis of Zn doped $Na_3Ni_2SbO_6$ cathode for Na-ion battery. *J. Power Sources* **336**, 186–195 (2016).
26. Kee, Y., Put, B., Dimov, N., Staykov, A. & Okada, S. Effects of Mn-doping on the Structural and Electrochemical Properties of $Na_3Ni_2SbO_6$ for Sodium-Ion Battery. *Batteries& Supercaps* **3**, 1–8 (2020).
27. Wang, C. *et al.* The top-down synthesis of sequentially controlled architectures for honeycomb-layered $Na_3Ni_2BiO_6$ towards high-voltage and superior performance cathodes for sodium-ion batteries. *J. Mater. Chem. A* **7**, 1797–1809 (2019).

28. Dai, H. *et al.* Unravelling the electrochemical properties and thermal behavior of $NaNi_{2/3}Sb_{1/3}O_2$ cathode for sodium-ion batteries by in situ X-ray diffraction investigation. *Electrochim. Acta* **257**, 146–154 (2017).
29. Kanyolo, G. M. *et al.* Honeycomb Layered Oxides: Structure, Energy Storage, Transport, Topology and Relevant Insights. *arXiv*:2003.03555 [cond-mat.str-el] (2020).
30. Wang, P. *et al.* An Ordered Ni_6 - Ring Superstructure Enables a Highly Stable Sodium Oxide Cathode. *Adv. Mater.* **31**, 1903483 (2019).
31. Evstigneeva, M. A., Nalbandyan, V. B., Petrenko, A. A., Medvedev, B. S. & Kataev, A. A. A new family of fast sodium ion conductors: $Na_2M_2TeO_6$ (M = Ni, Co, Zn, Mg). *Chem. Mater.* **23**, 1174–1181 (2011).
32. Sau, K. & Kumar, P. P. Role of Ion-Ion Correlations on Fast Ion Transport: Molecular Dynamics Simulation of $Na_2Ni_2TeO_6$. *J. Phys. Chem. C* **119**, 18030–18037 (2015).
33. Bianchini, F., Fjellvåg, H. & Vajeeston, P. Nonhexagonal Na Sublattice Reconstruction in the Super-Ionic Conductor $Na_2Zn_2TeO_6$: Insights from Ab Initio Molecular Dynamics. *J. Phys. Chem. C* **123**, 4654–4663 (2019).
34. Sau, K. & Kumar, P. P. Ion Transport in $Na_2Ni_2TeO_6$: Insights from Molecular Dynamics Simulation. *J. Phys. Chem. C* **119**, 1651–1658 (2015).
35. Sun, Y., Guo, S. & Zhou, H. Adverse effects of interlayer-gliding in layered transition-metal oxides on electrochemical sodium-ion storage. *Energy Environ. Sci.*, **12**, 825–840 (2019).
36. Delmas, C., Fouassier, C., Reau, J. –M. & Hagenmuller, P. Sur de nouveaux conducteurs ioniques a structure lamellaire. *Mat. Res. Bull.* **11**, 1081–1086 (1976).
37. Kumar, V., Bhardwaj, N., Tomar, N., Thakral, V. & Uma, S. Novel lithium-containing honeycomb structures. *Inorg. Chem.* **51**, 10471–10473 (2012).
38. Viciu, L. *et al.* Structure and basic magnetic properties of the honeycomb lattice compounds $Na_2Co_2TeO_6$ and $Na_3Co_2SbO_6$. *J. Solid State Chem.* **180**, 1060–1067 (2007).
39. Sankar, R. *et al.* Crystal growth and magnetic ordering of $Na_2Ni_2TeO_6$ with honeycomb layers and $Na_2Cu_2TeO_6$ with Cu spin dimers. *CrystEngComm* **16**, 10791–10796 (2014).
40. Bhardwaj, N., Gupta, A. & Uma, S. Evidence of cationic mixing and ordering in the honeycomb layer of Li_4MSbO_6 (M(iii) = Cr, Mn, Al, Ga) (S.G. C2/c) oxides. *Dalton Trans.* **43**, 12050–12057 (2014).

41. Kumar, V., Gupta, A. & Uma, S. Formation of honeycomb ordered monoclinic $Li_2M_2TeO_6$ (M = Cu, Ni) and disordered orthorhombic $Li_2Ni_2TeO_6$ oxides. *Dalton Trans.* **42**, 14992 (2013).
42. Gupta, A., Buddie Mullins, C. & Goodenough, J. B. $Na_2Ni_2TeO_6$: Evaluation as a cathode for sodium battery. *J. Power Sources* **243**, 817–821 (2013).
43. Berthelot, R. *et al.* New layered compounds with honeycomb ordering: $Li_3Ni_2BiO_6$, $Li_3NiM'BiO_6$ (M′ = Mg, Cu, Zn), and the delafossite $Ag_3Ni_2BiO_6$. *Inorg. Chem.* **51**, 5377–5385 (2012).
44. Berthelot, R., Schmidt, W., Sleight, A. W. & Subramanian, M. A. Studies on solid solutions based on layered honeycomb-ordered phases P2-$Na_2M_2TeO_6$ (M=Co, Ni, Zn). *J. Solid State Chem.* **196**, 225–231 (2012).
45. He, Z., Guo, W., Cui, M. & Tang, Y. Synthesis and magnetic properties of new tellurate compounds Na_4MTeO_6 (M = Co and Ni) with a ferromagnetic spin-chain structure. *Dalton Trans.* **46**, 5076–5081 (2017).
46. Karna, S. K. *et al.* Sodium layer chiral distribution and spin structure of $Na_2Ni_2TeO_6$ with a Ni honeycomb lattice. *Phys. Rev. B* **95**, 104408 (2017).
47. Zvereva, E. A. *et al.* Magnetic and electrode properties, structure and phase relations of the layered triangular-lattice tellurate Li_4NiTeO_6. *J. Solid State Chem.* **225**, 89–96 (2015).
48. He, Z., Cui, M. & Qiu, C. Synthesis, structure and magnetic behaviors of a new spin-1/2 chain compound Na_4CuTeO_6. *J. Alloys Compd.* **748**, 794–797 (2018).
49. Schmidt, W., Berthelot, R., Sleight, A. W. & Subramanian, M. A. Solid solution studies of layered honeycomb-ordered phases O3-$Na_3M_2SbO_6$ (M=Cu, Mg, Ni, Zn). *J. Solid State Chem.* **201**, 178–185 (2013).
50. Seibel, E. M. *et al.* Structure and magnetic properties of the α-$NaFeO_2$-type honeycomb compound $Na_3Ni_2BiO_6$. *Inorg. Chem.* **52**, 13605–13611 (2013).
51. Seibel, E. M., Roudebush, J. H., Ali, M. N., Ross, K. A. & Cava, R. J. Structure and magnetic properties of the spin-1/2-based honeycomb $NaNi_2BiO_{6-\delta}$ and its hydrate $NaNi_2BiO_{6-\delta}\cdot 1.7H_2O$. *Inorg. Chem.* **53**, 10989–10995 (2014).
52. Schmidt, W., Berthelot, R., Etienne, L., Wattiaux, A. & Subramanian, M. A. Synthesis and characterization of O3-$Na_3LiFeSbO_6$: A new honeycomb ordered layered oxide. *Mater. Res. Bull.* **50**, 292–296 (2014).
53. Mortemard de Boisse, B. *et al.* Intermediate honeycomb ordering to trigger oxygen redox chemistry in layered battery electrode. *Nat. Commun.* **7**, 11397 (2016).

54. Masese, T. *et al.* A high voltage honeycomb layered cathode framework for rechargeable potassium-ion battery: P2-type $K_{2/3}Ni_{1/3}Co_{1/3}Te_{1/3}O_2$. *Chem. Commun. (Camb)* **55**, 985–988 (2019).
55. Wang, P.-F. *et al.* Understanding the structural evolution and Na^+ kinetics in honeycomb-ordered O′3- $Na_3Ni_2SbO_6$ cathodes. *Nano Res.* **11**, 3258–3271 (2018).
56. Vaalma, C., Griffin, G. A., Buchholz, D. & Passerini, S. Non-Aqueous K-Ion Battery Based on Layered $K_{0.3}MnO_2$ and Hard Carbon/Carbon Black. *J. Electrochem. Soc.* **163**, A1295–A1299 (2016).
57. Pennycook, S. J. & Boatner, L. A. Chemically sensitive structure-imaging with a scanning transmission electron microscope. *Nature* **336**, 565–567 (1988).
58. Pennycook, S. J., Varela, M., Hetherington, C. J. D. & Kirkland, A. I. Materials Advances through Aberration-Corrected Electron Microscopy. *MRS Bull.* **31**, 36–43 (2006).
59. Pennycook, S. J. *et al.* Scanning Microscopy for Nanotechnology: Techniques and Applications (eds. Zhou, W. & Wang, Z.L.) 152–191 (Springer, 2006).
60. Xiao, L. *et al.* Insight into the Structural Disorder in Honeycomb-Ordered Sodium-Layered Oxide Cathodes. *iScience* **23**, 100898 (2020).
61. Shannon, R. D. Revised effective ionic radii and systematic studies of interatomic distances in halides and chalcogenides. *Acta Cryst.* A**32**, 751–767 (1976).
62. Li, X. *et al.* Insights into Crystal Structure and Diffusion of Biphasic $Na_2Zn_2TeO_6$. *ACS Appl. Mater. Interfaces* doi.org/10.1021/acsami.0c05863 (2020).
63. Kurbakov, A. I. *et al.* Long-range and short-range ordering in 2D honeycomb-lattice magnet $Na_2Ni_2TeO_6$. *J. Alloys Compd.* **820**, 153354 (2020).
64. Sandiumenge, F. A Multiscale Perspective on Misfit Dislocations in Oxide Films. *Front Mater.* **6**, 1–5 (2019).
65. Kanyolo, G. M. & Masese, T. An Idealised Approach of Geometry and Topology to the Diffusion of Cations in Honeycomb Layered Oxide Frameworks. doi.org/ 10.26434/*chemrxiv*.11961123.v3 (2020).
66. Gabrisch, H., Yazami, R. & Fultz, B. The Character of Dislocations in $LiCoO_2$. *Electrochem. Solid-State Lett.* **5**, A111–A114 (2002).
67. Wang, H., Jang, Y. –I., Huang, B., Sadoway, D. R. & Chiang, Y. –M. TEM Study of Electrochemical Cycling-Induced Damage and Disorder in $LiCoO_2$ Cathodes for Rechargeable Lithium Batteries. *J. Electrochem. Soc.* **146**, 473–480 (1999).
68. Singer, A. *et al.* Nucleation of dislocations and their dynamics in layered oxide cathode materials during battery charging. *Nat. Energy* **3**, 641–647 (2018).
69. Allendoerfer, C. B. & Weil, A. The Gauss-Bonnet Theorem for Riemannian

Polyhedra. *Trans. Amer. Math. Soc*. **53**, 101–129 (1943).
70. Petříček, V. Dušek, M. & Palatinus, L. Crystallographic Computing System JANA2006: General features. *Z. Kristallogr.* **229**, 345–352 (2014).
71. Momma, K. & Izumi, F. VESTA 3 for three-dimensional visualization of crystal, volumetric and morphology data. *J. Appl. Crystallogr.* **44**, 1272–1276 (2011).

Author contributions

T. M. and H. S. contributed to the syntheses of the materials. Y.M., T.S., M.I. and T.T. performed the morphological characterisation of the materials using TEM. Y.M., G.K., T.M, H.S. and T.S. wrote the manuscript. G.K. and T.M. designed the graphic illustrations outlined in the work. G.K., H.S., T.M. and Y.M. provided input with the data analyses, helped with the discussion and assisted with the manuscript correction. T.T., M. I. and T.S. made the initiative to undertake this work. All authors have given approval to the final version of the manuscript.

Acknowledgements

T.M. thanks Ms. Shinobu Wada and Mr. Hiroshi Kimura for the unrelenting support in undertaking the entire study. T. M. also gratefully acknowledges Ms. Kumi Shiokawa, Mr. Masahiro Hirata and Ms. Machiko Kakiuchi for their advice and technical help as we conducted the syntheses, electrochemical and XRD measurements. This work was conducted in part under the auspices of the Japan Society for the Promotion of Science (JSPS KAKENHI Grant Number 19K15685), Sumika Chemical Analyses Services (SCAS) Co. Ltd., National Institute of Advanced Industrial Science and Technology (AIST) and Japan Prize Foundation.

Competing interests

The authors declare no competing interests.

Data availability

Supplementary information will be availed online (access link to be appended during production).